JGR Solid Earth

RESEARCH ARTICLE
10.1029/2021JB021723

Radiometric Temperature Determination in Nongray Bridgmanite: Applications to Melting Curve and Post-Perovskite Transition Boundary in the Lower Mantle

Sergey S. Lobanov[1,2], Sergio Speziale[1], Jung-Fu Lin[3], Lukas Schifferle[1,2], and Anja Schreiber[1]

[1]GFZ German Research Centre for Geosciences, Telegrafenberg, Potsdam, Germany, [2]Insitute of Geosciences, University of Potsdam, Karl-Liebknecht-Straße, Potsdam, Germany, [3]Department of Geological Sciences, Jackson School of Geosciences, The University of Texas at Austin, Austin, TX, USA

Key Points:

- Thermal radiation spectra record a nongray interaction with bridgmanite in laser-heated diamond anvil cells
- Radiometric temperature of nongray bridgmanite in laser-heated diamond anvil cells is up to 5%–10% off the maximum sample temperature
- Extant melting curves and experimental phase transition boundaries in the bridgmanite system contain this systematic error in temperature

Supporting Information:

Supporting Information may be found in the online version of this article.

Correspondence to:

S. S. Lobanov,
slobanov@gfz-potsdam.de

Citation:

Lobanov, S. S., Speziale, S., Lin, J.-F., Schifferle, L., & Schreiber, A. (2021). Radiometric temperature determination in nongray bridgmanite: Applications to melting curve and post-perovskite transition boundary in the lower mantle. *Journal of Geophysical Research: Solid Earth*, *126*, e2021JB021723. https://doi.org/10.1029/2021JB021723

Received 15 JAN 2021
Accepted 5 APR 2021

Abstract Experiments in laser-heated diamond anvil cells (LH DACs) are conducted to assess phase diagrams of planetary materials at high pressure-temperature (*P-T*) conditions; thus, reliable determination of temperature in LH DAC experiments is essential. Radiometric temperature determination in LH DACs relies on the assumption of sample's wavelength-independent optical properties (graybody assumption), which is not justified for major lower mantle materials. The result is that experimental phase diagrams contain systematic unconstrained errors. Here we estimate the systematic error in radiometric temperature of nongray polycrystalline bridgmanite (Bgm; $Mg_{0.96}Fe^{2+}_{0.036}Fe^{3+}_{0.014}Si_{0.99}O_3$) in a LH DAC by modeling emission and absorption of thermal radiation in a sample with experimentally-constrained optical properties. A comparison to experimental data validates the models and reveals that thermal spectra measured in LH DAC experiments record the interaction of radiation with the hot nongray sample. The graybody assumption in the experiments on translucent Bgm (light extinction coefficient, $k < \sim 250$ cm^{-1} at 500–900 nm) yields temperatures ~5% higher than the maximum temperature in the sample heated to ~1900 K. In contrast, the graybody temperature of dark Bgm ($k > \sim 1500$ cm^{-1}), such as that produced upon melt quenching in LH DACs, underestimates the maximum temperature by ~10%. Our experimental results pose quantitative constraints on the effect of nongray optical properties on the uncertainty of radiometric temperature determination in Bgm in the LH DACs. Evaluating nongray temperature in the future would enable a revision of the Bgm to post-perovskite phase transition and the high-pressure melting curve of Bgm.

Plain Language Summary We modeled how the color of Earth's most abundant mineral (bridgmanite) affects temperature measurements in laser-heated diamond anvil cell experiments with implications to the phase diagram of bridgmanite. We show that, depending on the optical properties of bridgmanite, temperature determination in such experiments may either systematically overestimate or underestimate the maximum temperature by up to 5%–10% due to the wavelength-dependent emission and absorption in the hot sample. Overall, this study shows the phase boundaries in the bridgmanite system need revision.

1. Introduction

Measurements of the properties of minerals and rocks at high pressure-temperature (*P-T*) conditions advance our understanding of planetary interiors. A common experimental approach is to recreate the *P-T* conditions of interest in a laser-heated diamond anvil cell (LH DAC), where a small (~10–100 μm) sample is squeezed between the tips of two diamonds and heated with IR (infra-red) lasers. This technique grants routine access to the thermodynamic conditions of planetary mantles and cores with the sample accessible to interrogation by a variety of optical, x-ray, and electrical probes (Geballe et al., 2020; Holtgrewe et al., 2019; Ohta et al., 2012; Petitgirard et al., 2014; Shen & Mao, 2017). LH DAC studies of phase diagrams are particularly important as these can be compared to seismic discontinuities characteristic of the mantle and core. For example, the melting (solidus) temperature of lower mantle phases places an upper limit on the temperature at the core-mantle boundary as the overlying mantle is mostly solid (Andrault et al., 2011; Fiquet et al., 2010; Nomura et al., 2014). Similarly, the *P-T* slope of the phase boundary between bridgmanite (Bgm)

and post-perovskite (Ppv) corroborates the Ppv interpretation (Murakami et al., 2004; Oganov & Ono, 2004) of the D″ shear-wave velocity increase and splitting anisotropy (Garnero, 2000; Moore et al., 2004; Sidorin et al., 1998). Both these examples have implications for placing constraints on the temperature gradient in the thermal boundary layer above the core and heat flow across the core-mantle boundary (Hernlund et al., 2005; Lay et al., 2008; van der Hilst et al., 2007).

In spite of major advantages of the LH DAC method, accurate characterization of experimental temperatures at high pressures is challenging. Direct measurements of sample's temperature in a LH DAC (e.g., by a thermocouple) are not yet possible because of severe radial and axial temperature gradients intrinsic to the LH DAC method (Kiefer & Duffy, 2005; Montoya & Goncharov, 2012; Panero & Jeanloz, 2001; Rainey et al., 2013). Instead, sample's T is usually inferred indirectly by fitting Planck's law to the measured spectrum of thermal radiation emitted by the heated sample (Benedetti et al., 2007; Benedetti & Loubeyre, 2004; Campbell, 2008; Du et al., 2013; Giampaoli et al., 2018; Heinz & Jeanloz, 1987a, 1987b; Jeanloz & Heinz, 1984; Kavner & Panero, 2004; Kunz et al., 2018; Walter & Koga, 2004). Two important assumptions are implicit in radiometric temperature determination in LH DACs: (i) graybody assumption and (ii) peak temperature approximation. The first one is that the sample's emissivity (and absorptivity) is wavelength-independent at ~600–900 nm, the spectral range commonly employed for radiometric temperature measurements. All major iron (Fe)-bearing lower mantle minerals (Bgm, Ppv, ferropericlase) have absorption bands in this spectral range (Goncharov et al., 2006, 2010; Keppler et al., 1994). Therefore, as emissive and absorptive power of a body at a given wavelength are equal (Kirchhoff's law (Kirchhoff, 1860, 1861)), the graybody assumption for Fe-bearing phases is formally not justified. Unfortunately, the temperature-dependence of absorption bands of lower mantle minerals remains unknown, which means that their emissivity in LH DAC experiments is unconstrained. If the emissivity at high P-T is strongly wavelength-dependent, then the systematic error associated with the graybody assumption may be large, up to 15%–20% of the maximum T in the sample (Deng et al., 2017; Deng & Lee, 2017; Lobanov & Speziale, 2019). The second assumption is that the fitted temperature corresponds to the maximum temperature in the sample. This is valid to first order as, according to the Stefan-Boltzmann law, the total radiated energy of a blackbody in vacuum is proportional to the fourth power of its temperature (Boltzmann, 1884; Stefan, 1879). That is, the contribution of the hottest part of the sample to the measured thermal radiation spectrum is the strongest. However, along the axial temperature gradient a sample with nonzero absorptivity attenuates the thermal emission from the hottest spot and emits light of a colder temperature thereby modifying intensities in the recorded spectrum. Radial temperature gradients also contribute to the total spectrum collected by the detector (Manga & Jeanloz, 1996; Panero & Jeanloz, 2001). The result is that the apparent (fitted) temperature is systematically lower than the maximum temperature of the heated sample.

These two sources of systematic errors in apparent temperature are recognized (Deng et al., 2017; Kavner & Panero, 2004; Kunz et al., 2018; Manga & Jeanloz, 1996; Panero & Jeanloz, 2001; Rainey and Kavner, 2014) but quantitative estimates of their magnitude require that the wavelength-, pressure-, and temperature-dependence of the sample's absorption coefficient are established. In this work, we address systematic errors implicit in temperature determination in a synthetic sample of Fe-bearing Bgm, a silicate perovskite-structured mineral with a chemical formula of $Mg_{0.96}Fe^{2+}_{0.036}Fe^{3+}_{0.014}Si_{0.99}O_3$ that closely approximates the phase representing ~80 vol% of the Earth's lower mantle (Irifune et al., 2010; Wang et al., 2015). We employ conventional and time-resolved optical spectroscopy experiments to constrain the emissive and absorptive power of Bgm at lower mantle conditions and use them to model the emission and absorption of light in a LH DAC experiment. The models agree with direct experimental observations and offer a quantitative estimate of the systematic error in graybody temperatures pertaining to measurements on Bgm in LH DACs. Overall, the results of our work call for a revision of the uncertainties associated with Bgm-Ppv phase boundary and the Bgm solidus curve.

2. Materials and Methods

2.1. Laser-Heating Diamond Anvil Cell Experiment

The sample studied here is a polycrystalline bridgmanite (Bgm; grain size of 2–4 μm) synthesized in a multi-anvil press (run# 5K2694) as reported by Fu et al. (2018). Electron microprobe and Mössbauer analysis identified the sample chemical composition as $Mg_{0.96}$ $Fe^{2+}_{0.036}Fe^{3+}_{0.014}Si_{0.99}O_3$ (Fu et al., 2018). The sample

was double-side polished to a thickness of ~25 μm and then loaded into a hole drilled in a rhenium gasket between two slabs of dry KCl. Immediately after the loading, the DAC was sealed and pressure increased to ~50 GPa as estimated from the spectral position of the high-frequency edge of the Raman diamond peak (Akahama & Kawamura, 2006). Once at high pressure, the sample was double-side heated by a continuous-wave 100 W 1070 nm YLR-100-AC (IPG Photonics) Yb fiber laser with a nearly flat-top intensity distribution and beam size of ~10 μm in the focal plane (Lobanov, Schifferle, et al., 2020). Thermal radiation was collected simultaneously from both sides by 20× Mitutoyo Plan Apochromat NIR objectives and passed through two identical spatial filters (each made of two achromatic doublets and a confocal pinhole), which allowed reducing the thermally-probed region to a circular spot with a diameter of ~10 μm and minimizing the systematic error in T due to radial temperature gradients. Thermal images of both sides of the sample were projected together with a vertical offset of ~2 mm onto the entrance slit of a dual-output SpectraPro HRS-300 spectrograph (Princeton Instruments), dispersed by a diffraction grating (300 groves/mm; blaze wavelength: 500 nm), and recorded simultaneously by a PIXIS-256 CCD camera. The spectral response of the thermal radiation collection path was calibrated by a using a Conrad Electronics halogen lamp set to 2318 K. The dependence of spectral temperature on electric current was calibrated against a NIST-traceable bulb at P02.2. beamline (Deutsches Elektronen-Synchrotron DESY). The wavelength calibration of the CCD camera was achieved by placing an Hg atomic emission light source at the entrance slit of the spectrograph. Two regions of the CCD images that recorded the thermal emission spectra from the two sides of the sample were binned, exported, and analyzed for temperature.

2.2. Optical Absorption Measurements at 1 atm and 300 K

The total light extinction coefficient (absorption + scattering coefficients) of a free-standing (1 atm/300 K) 25 ± 0.3 μm thick polycrystalline Bgm (same as in LH DAC experiments) was measured with a tungsten light source on a Bruker Hyperion 2000 all-reflective microscope attached to a Bruker VERTEX 80v FTIR spectrometer equipped with a broadband CaF_2 beamsplitter and a room-temperature Si-diode detector and evaluated as:

$$k(\lambda) = -\frac{t}{\ln_{10}} \times log_{10}^{\frac{I_{sample}(\lambda)}{I_{reference}(\lambda)}} = \alpha(\lambda) + s(\lambda) \quad (1)$$

where λ is wavelength, I_{sample} and $I_{reference}$ are probe intensities recorded through the sample and optical reference (a glass slide), respectively, and t is sample thickness inferred from the spectral separation of interference fringes scaled by the direction-averaged refractive index of pure $MgSiO_3$-Bgm at 1 atm (Yeganeh-Haeri, 1994). The right hand side of Equation 1 shows that in polycrystalline samples the measured total extinction coefficient is a sum of absorption (α) and scattering (s) coefficients.

2.3. Optical Absorption Measurements in a Laser-Heated Diamond Anvil Cell

Optical properties of our Bgm at ~50 GPa were probed by a pulsed (1 ns/250 kHz) broadband supercontinuum laser (Leukos NewWave) both at 300 K and at high temperature. The probe laser was injected into the optical path of the laser-heating instrument described in Section 2.1 and focused to a spot of ~5 μm in diameter on the sample. The transmitted portion of the probe radiation was recorded by a gated PI-MAX 4 Intensified CCD (ICCD) detector (3 ns gate) installed on the second optical output of the SpectraPro HRS-300 spectrograph. Detailed description of this experimental setup is provided in Section II (Optical Setup) of Lobanov, Schifferle, et al. (2020). The use of the gated detector allows for precise synchronization to the probe laser pulses and is very effective in reducing the amount of thermal radiation that arrives to the ICCD, enabling optical measurements up to ~2000 K (Lobanov et al., 2016; Lobanov et al., 2017). The total light extinction coefficient was evaluated using Equation 1 after subtracting thermal and dark current contributions from the I_{sample} (collected upon heating while blocking the probe supercontinuum laser) and $I_{reference}$ (collected through KCl) signals. Cutting across the decompressed sample with a focused ion beam allowed estimating the gasket and sample thicknesses as input parameters to the 1-D radiation transport model described below (Figure S1).

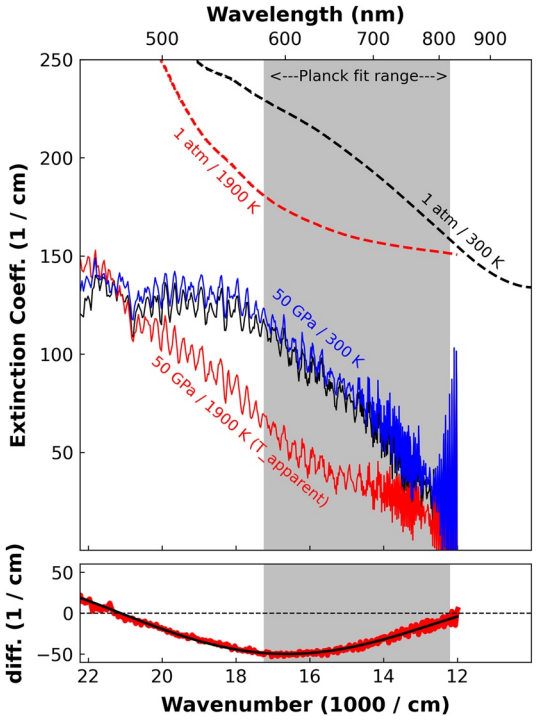

Figure 1. Top: Extinction coefficients, $k(\lambda)$, of 5K2694 Bgm, ($Mg_{0.96}Fe^{2+}_{0.036}Fe^{3+}_{0.014}Si_{0.99}O_3$), measured at 1 atm and 300 K (black dashed curve), as well as at ~ 50 GPa before, upon, and after laser heating to the apparent temperature of ~1900 K (black, red, blue curves, respectively). Bottom: Difference curve (red) in cm^{-1} and its polynomial fit (black) obtained by subtracting the average of the room-temperature spectra at 50 GPa from the high-temperature spectrum at 50 GPa. The red dashed curve in the Top panel is a hypothetical extinction coefficient of Bgm at 1 atm and ~1900 K obtained by adding the difference curve obtained at 50 GPa and ~1900 K to the room-temperature spectrum at 1 atm.

2.4. 1-D Radiation Transport Model

To model the total thermal spectrum collected by the detector ($I_{detector}$) we employ the previously developed one-dimensional thermal radiation transport model for LH DAC (Lobanov & Speziale, 2019). Briefly, we model an axially-symmetric DAC cavity (thickness of $2d$ μm) where the center of an absorbing sample ($2z$ μm thick) is placed at the center of the cavity and surrounded by two layers of a nonabsorbing pressure medium (each layer is $d-z$ μm thick, see Figure S1). The temperature at the center of the sample is set to T_{max} and a parabolic axial temperature gradient is assigned, characteristic of a sample with constant thermal conductivity (Manga and Jeanloz, 1996), with the temperature at the diamond culet fixed to 300 K (Kiefer & Duffy, 2005; Montoya and Goncharov, 2012). The geometry and input temperature profile are similar to those used previously (see Figure 1 in (Lobanov & Speziale, 2019)) and represent a dielectric sample in a DAC cavity laser-heated from both sides by a near-IR heating laser (e.g., Nd:YAG or Nd:YLF).

Half of the DAC cavity is evenly sliced into $n = 10^3$ slabs and an individual temperature is assigned to each slab (Ti, $i = 1, ..., n$) based on the parabolic axial temperature profile. Thermal emission of the ith slab is then given by Planck's law of blackbody radiation scaled by the slab's emissivity:

$$I_i(\lambda) = \epsilon_i(\lambda)\frac{2hc^2}{\lambda^5}\frac{1}{e^{\frac{hc}{\lambda kT_i}}-1} \quad (2)$$

where $\epsilon_i(\lambda)$ is wavelength-dependent emissivity, c, h, and k are the speed of light, Planck, and Boltzmann constants, respectively. The emissivity is given by Kirchhoff's law for partially transparent bodies (McMahon, 1950):

$$\epsilon_i(\lambda) = 1 - 10^{-\alpha(\lambda)\times\frac{\left(\frac{d}{n}\right)}{\ln 10}} \quad (3)$$

The large number of slabs (n) ensures a local thermal equilibrium, which is necessary for the application of Kirchhoff's law. Please note that light scattering in a polycrystalline sample may be substantial; thus, using experimentally-constrained $\alpha(\lambda)$ in Equation 3 requires subtracting the contribution of scattering from the total light extinction coefficient via Equation 1. We assume the pressure medium to be strictly nonabsorbing in the modeled spectral range, which allows us to set its emissivity to zero. This is reasonable as many pressure media used in LH DAC studies (e.g., KCl, Al_2O_3, MgO) are wide bandgap insulators and do not absorb in the visible and near-IR range. Even though these insulators may emit in the visible and near-IR due to defects, their emissivity would be negligible compared to that of absorbing Bgm considered here (Touloukian & DeWitt, 1972).

Light propagation in the modeled sample is governed by emission, absorption, and scattering within individual slabs:

$$I^*_{i+1}(\lambda) = \left(I^*_i(\lambda) + I_i(\lambda)\right)\times 10^{A_i} \quad (4)$$

where $I^*_{i+1}(\lambda)$ is the thermal emission spectrum that is passed to the next ($i+1$) slab after light emission and attenuation in the ith slab (see Figure 1, inset in Lobanov & Speziale, 2019) and A_i is ith slab absorbance:

$$A_i(\lambda) = 10^{-k(\lambda)\times\left(\frac{d}{n}\right)/\ln 10} \quad (5)$$

Note that unlike $\epsilon_i(\lambda)$ in Equation 3, A_i is evaluated from the total measured light extinction coefficient (k) as both absorption and scattering contribute to light attenuation within the sample. Although the geometry represents half of the DAC cavity, the contribution from the second modeled half is also computed (Lobanov & Speziale, 2019). The resulting total spectrum ($I_{detector}$) is fitted to Planck's law under the graybody assumption, yielding $T_{apparent}$ and a single value of emissivity for a given T_{max}. The value of T_{max} is a free parameter in the 1-D Radiation Transport Model and is adjusted manually to reproduce the apparent temperature observed in the experiment. The graybody fit to $I_{detector}$ simulates a common LH DAC experiment with radiometric temperature measurements in a sample with unconstrained optical properties. The difference between $T_{apparent}$ and T_{max} is thus a quantitative estimate of the systematic error in the temperature determination due to sample's general (nongray) optical properties.

3. Results

3.1. Optical Properties of Translucent Bridgmanite

Modeling thermal emission and its propagation in a nongray sample require that the wavelength-dependence of the sample's absorption and scattering coefficients are established in the spectral range of interest. Toward that end, we measured the total extinction coefficient of a free-standing Bgm sample (1 atm/300 K). The measured extinction coefficient of our polycrystalline Bgm sample (Figure 1, black dashed curve) shows a distinct slope and a broad absorption band centered at ~665 nm. Based on its position and width (Mattson & Rossman, 1987), this band is assigned to a Fe^{2+}-Fe^{3+} charge transfer (CT), in agreement with previous optical studies of Bgm (Keppler et al., 1994). The overall slope of the Bgm extinction coefficient at 1 atm and 300 K is likely related to the Fe-O CT, but scattering also contributes to the apparent extinction due to the polycrystalline nature of the studied sample. The main advantage of the optical measurements on a free-standing Bgm sample is that the associated uncertainty in the magnitude of the extinction coefficient is small. This is primarily due to a thick (25 μm), flat, and relatively homogeneous sample as well as a highly-transparent optical reference. Several measurements at distinct sample positions yielded extinction coefficients within ~15%, which we attribute to sample heterogeneity.

Increasing pressure blue-shifts the Fe^{2+}-Fe^{3+} CT band, and at ~50 GPa the band is centered at ~605 nm (Figure 1), in agreement with previous optical studies of Bgm at high pressure (Goncharov et al., 2015; Keppler et al., 2008). Upon heating at ~50 GPa, the intensity of the Fe^{2+}-Fe^{3+} CT decreases continuously and at T ~1900 K (apparent temperature) this band is no longer discernible in the spectrum. (Please note that we need to refer to the measured T as apparent T because it was obtained under the graybody assumption and its relation to the maximum temperature in the sample is unknown.) The observed magnitude of the extinction coefficients measured at 50 GPa underestimates sample's opacity by approximately a factor of two because previous high-pressure study of single crystalline Bgm (at 300 K) showed that the magnitude of Bgm absorption coefficient is insensitive to pressure (Goncharov et al., 2015). The reason to this underestimation is likely in the imperfect optical referencing: visual observations of the sample cavity reveal that KCl is slightly scattering in the visible range (tentatively, due to uniaxial stress field in the DAC). Another consequence of imperfect referencing is the decreased contrast in absorptivity between the highly transparent Bgm and KCl, resulting in noisy spectra. Nonetheless, the recorded temperature-induced variation in sample's absorbance at 50 GPa is reliable because it is related only to the realtive change in transmittance of Bgm upon heating. That is, our optical measurements at 50 GPa enable an estimate of the absolute change in the light extinction coefficient upon heating from 300 to ~1900 K but do not offer a reliable spectrum that can be used in the radiation transport modeling. To circumvent this problem, we sum the difference curve (Figure 1, bottom), which shows the absolute temperature-induced change in the extinction coefficient at 50 GPa, with the high-quality extinction coefficient of the same Bgm measured at 1 atm to produce a hypothetical light extinction coefficient at 1 atm and ~1900 K (Figure 1, red dashed curve). This high-temperature correction is qualitatively appropriate because (i) the pressure-induced blue-shift of the Fe^{2+}-Fe^{3+} CT is small (~60 nm and was not corrected for) and (ii) the intensity of this band is not sensitive to pressure (Goncharov et al., 2015; Keppler et al., 2008).

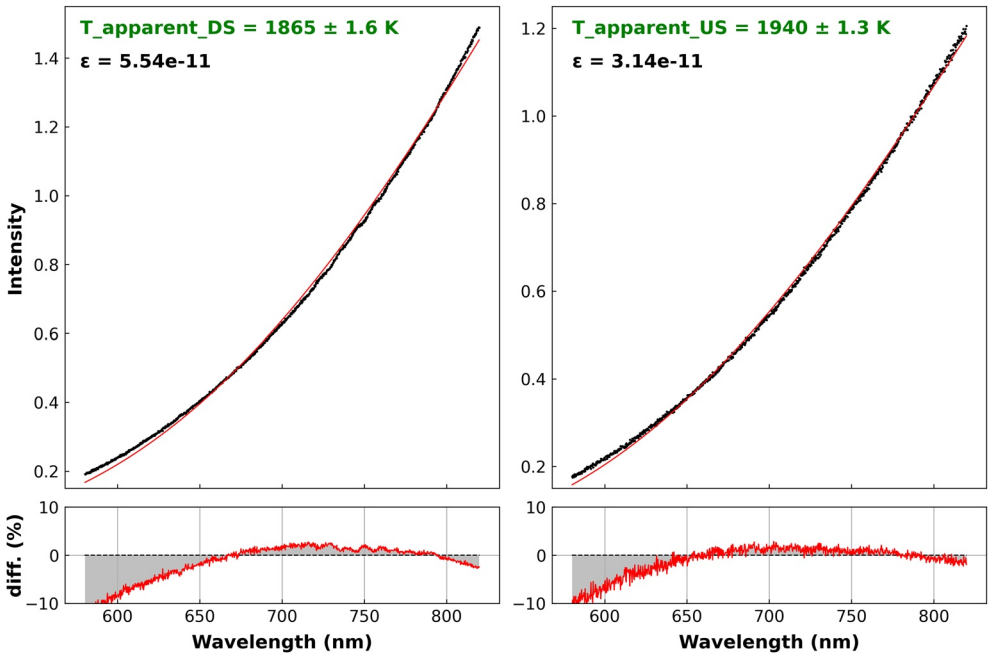

Figure 2. Experimental thermal radiation spectra of 5K2694 bridgmanite at ~50 GPa in a double-sided laser-heated (Yb-fiber laser) diamond anvil cell and corresponding constant-emissivity (ε) Planck fits. The difference in the fitted values of emissivity is solely due to the different optical responses of the downstream (DS) and upstream (US) legs (relative to the supercontinuum light source). Left: DS side. Right: US side. Bottom: Difference curves (fit/measured − 1) in %. Planck fitting at 650–820 nm produces a very similar difference curve but yields slightly ~30 K lower apparent temperatures.

3.2. Radiometric Temperature Determination in Translucent Bridgmanite

Figure 2 shows constant emissivity (wavelength-independent) Planck fits to the observed thermal emission spectra collected in the course of the high-temperature optical measurements at ~50 GPa reported above. Averaging the apparent (fitted) temperature from both DAC sides yields ~1900 K. The very small (1–2 K) statistical (standard deviation) uncertainties on the fitted temperature for the two individual spectra are typical of LH DAC experiments. However, a closer examination of the fits and the difference curves (Figure 2, bottom), which were evaluated as $\left(\frac{\text{Planck fit}}{\text{Measured}} - 1\right) \times 100\,\%$, reveals that Planck functions fitted to the downstream (DS) and upstream (US) data systematically underestimate the observed intensity at low ($\lambda < 670$ nm) and high ($\lambda > 790$ nm) wavelengths while overestimate it in the middle of the spectral range ($670 < \lambda < 790$ nm). The largest differences are of the order of 10% at ~580 nm. The wavelengths at which the DS and US difference curves change sign are strikingly similar, suggesting that the cause for the residuals in DS and US data is fundamentally the same.

Light emission and absorption in our Bgm sample at 50 GPa are modeled as described above by adjusting T_{max} to yield $T_{apparent} = 1900$ K and geometrical parameters fixed to $d = 11$ μm (half of the measured diamond-to-diamond distance) and $z = 5.4$ μm (both measured in the decompressed sample, Figure S1). Prior to investigating nongray behavior, we tested whether the experimentally-observed deficiencies in the Planck fit are due to the spectroscopic sampling of colder parts of the sample along the axial temperature gradient. This was realized by setting α to a constant (100, 200, and 300 cm^{-1}), which yields wavelength-independent emissivity via Equation 3. Here, modeling at different α (albeit gray) is necessary because it alters the spectroscopic contribution of colder regions to $I_{detector}$. All these models reproduced the shape of the difference curves plotted in Figure 2 but their amplitude was ~20 times smaller than that observed in the experiment under any reasonable input parameters (d, z, input axial T profile). Similarly, the radial temperature gradient, which is not as steep as the axial, produces difference curves with amplitude at least ~50 times smaller

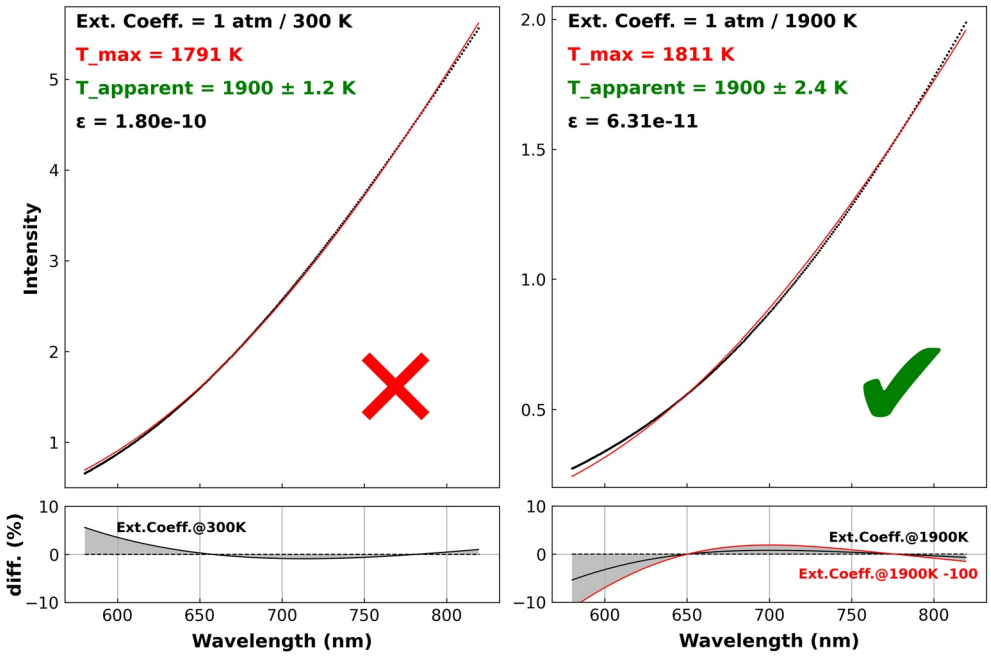

Figure 3. Constant-emissivity (ε) Planck fits (red curves) to modeled thermal radiation spectra (black dotted curves) computed assuming nongray emission and extinction in 5K2694 Bgm with experimentally-constrained extinction coefficient at 1 atm and 300 K (left) and calculated extinction coefficients at 1 atm and ~1900 K ($T_{apparent}$) after the wavelength-independent scattering correction of −100 cm^{-1} (right). Bottom: Difference curves (fit/modeled − 1) in percentage. Black and red curves are difference curves produced using the different extinction coefficients as labeled.

than that observed in the experiment (Figure S2). Based on this quantitative assessment, we conclude that both axial and radial T gradients do not explain the residual observed in the experiment.

We also need to consider whether chromatic aberrations due to the use of refractive optics in our experimental setup contribute to the difference curve. We minimize chromatic aberrations by (i) using a plan apochromatic objective to collect the thermal radiation from the sample as well as (ii) a nearly flat-top heating laser profile which helps homogenizing the temperature across the field of view of the spatial filter (although we note that the temperature is not strictly constant across the field of view and a radial temperature gradient is present). Statistical uncertainties in Planck fitting (standard deviation) may indicate the extent to which chromatic aberrations contribute error to radiometric temperature determination (Walter & Koga, 2004). In the present case, the statistical uncertainties are small (<2 K); thus, we conclude that chromatic aberrations in our experimental setup are minimal. We also note that the difference curves that are typical of chromatic aberrations (Walter & Koga, 2004) are opposite in sign to that observed in our work, which supports our view that the effect of chromatic aberrations on the experimentally observed difference curves is unimportant. To further confirm this, we laser-heated a flat *hcp*-Fe foil (although not an ideal graybody (Seagle et al., 2009)) at P ~30 GPa to T ~2000 K and found that indeed the difference curve, which we presume is entirely due to minor chromatic aberrations in this test case, is opposite in sign to that in the case of our Bgm sample (Figure S3). We show in the following that the wavelength-dependent optical properties of Bgm provide a much more viable explanation for the observed difference curve.

To depart from constant emissivity, we assumed that light scattering in our Bgm sample is negligible ($s(\lambda) << k(\lambda)$) as a starting scenario, which grants computing the wavelength-dependent emissivity (Equations 1 and 3) and light attenuation in the heated sample (Equations 4 and 5). (Below, however, we quantitatively estimate the scattering coefficient while treating it as an adjustable parameter.) In the first case, we modeled the optical properties of the sample by the extinction coefficient of Bgm measured at 1 atm and 300 K (Figure 1, black dashed curve). Figure 3 (left) shows the results of this case presented as a graybody Planck fit (red curve) to the modeled thermal emission spectrum ($I_{detector}$, black dotted curve). Key features of the Planck fit are (i) $T_{max} = 1791$ K (i.e., $T_{apparent} - 109$ K) and (ii) the sign of the difference curve opposite to that

in the experiment (Figure 3 bottom left vs. Figure 2 bottom panels). The higher apparent temperature makes sense as the slope of the assumed absorption coefficient implies that the emitted spectrum is bluer (i.e., hotter) than that emitted by a graybody at T_{max}. The sample, however, is too transparent and thin to attenuate this extra blue light. The failure to reproduce the sign of the experimental difference curve suggests that the convex-like shape of the absorption coefficient at 1 atm/300 K (Figure 1, black dashed curve) is inadequate for modeling the optical properties of Bgm at ~1900 K.

In the second case, we tested whether using the temperature-corrected extinction coefficient (1 atm/1900 K; Figure 1, red dashed curve) would reproduce the experimental data. Clearly this model is more successful. The sign and shape of the difference curve are now correct but the amplitude is approximately half of that in experiment (Figure 3, bottom right, green). We assessed the model response to the assumed axial T profile by changing the parabolic temperature gradient to a linear one and found T_{max} = 1888 K (i.e., $T_{apparent}$ − 12 K). In this case, however, the difference curve was almost unaffected with only slightly higher amplitude (by ~8% than in the case with parabolic T profile). Modifying sample thickness within ±5% produced $T_{apparent}$ within 1 K off 1900 K. The only model parameter that markedly affects the amplitude of the difference curve is sample's emissivity. A subtraction of 100 cm^{-1} from the temperature-corrected extinction coefficient (k) to obtain the absorption coefficient (α) in order to evaluate emissivity via Equation 3, produces a difference curve that matches not only the shape but also the amplitude of the difference curves observed in experiment (Figure 3, bottom right, red in comparison with Figure 2, bottom). The physical meaning of this subtraction is that it corrects the measured extinction coefficient for scattering in our polycrystalline Bgm: $\alpha(\lambda) = k(\lambda) - s(\lambda)$, which is necessary to adequately model sample's emissivity. The assumption of a relatively small and constant scattering coefficient across the 580–820 nm spectral range is reasonable because for $\lambda < 1000$ nm and grain size of ~3 μm (i) Mie scattering is (almost) exclusively in the forward direction (i.e., scattered light ends up on the detector) and (ii) the wavelength-dependence in non-forward scattering component (i.e. light that does not reach the detector) is small (Hulst, 1957).

In the present case of a translucent sample, the nongray behavior of Bgm results in the overestimation of the maximum temperature in the sample by ~5%. That is, in the limit of < 2000 K, the systematic error in T due to nongray optical properties of translucent Bgm is comparable to the typically assumed ambiguity in the radiometric temperature determination of 50–150 K. The significance of the present case is that it positively demonstrates that sample's wavelength-dependent optical properties may leave a clear record in the measured thermal emission spectrum, which can be revealed by analyzing small but systematic deficiencies in Planck fitting under the graybody assumption.

3.3. Optical Properties of Dark Bridgmanite

Melting of Bgm and other Bgm-bearing samples in LH DAC experiments typically produces a dark circular feature upon crossing the solidus (Andrault et al., 2014; Zerr & Boehler, 1993). The darker appearance of the heated spot is likely related to (i) its elevated iron content as iron fractionates into the melt (Andrault et al., 2017; Heinz & Jeanloz, 1987a; Nomura et al., 2014) and (ii) increased contribution of the non-forward light scattering component (i.e., light that does not reach the detector) in the submicron-grained quenched sample. To model the important scenario of radiometric determination of melting temperatures in LH DACs, we reproduced such a dark circular feature by melting our Bgm sample at ~50 GPa (Figure 4, left insets). No chemical reactions were observed by synchrotron x-ray diffraction (XRD) after quenching the sample to 300 K because only Bgm and KCl are present in the XRD pattern (Figure S4). Le Bail refinement of the XRD pattern suggests that the quenched sample is mostly crystalline because no diffuse signal is apparent in the difference curve. After the synthesis, the average light extinction coefficient of this dark Bgm was measured at 300 K using the supercontinuum laser. Please, note that the diameter of the focused supercontinuum laser is approximately two times smaller than that of the circular dark feature itself; thus, the laser adequately probes light attenuation in the quenched sample.

We obtained the extinction coefficient of Bgm at 50 GPa via Equation 1 after measuring the thickness of the laser-heated spot of the recovered sample (Figure S1). Note that here we did not account for elastic thickening of Bgm upon decompression as such a correction would be small (~5%). Also, we assume that the resulting quenched sample is optically homogeneous (i.e., the absorption and scattering coefficients do not change across the sample). The obtained light extinction coefficient (Figure 4, right inset) is ~5–10

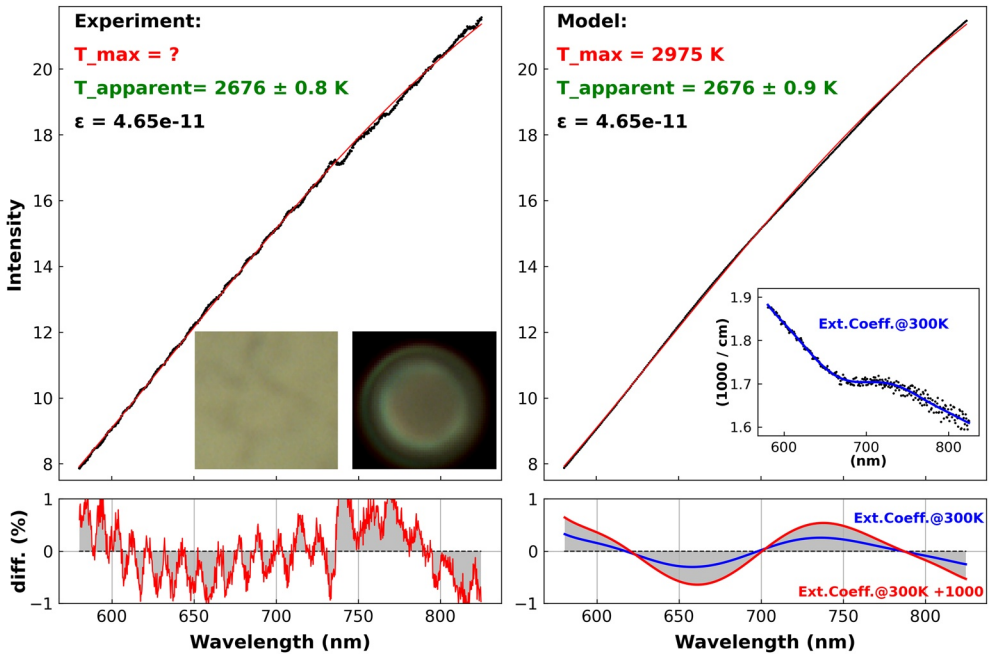

Figure 4. Constant-emissivity (ε) Planck fits to measured (left) and modeled (right) thermal radiation of dark bridgmanite at ~50 GPa in a double-sided laser-heated diamond anvil cell. Bottom: Difference curves (fit/measured or modeled − 1) in %. Blue and red curves are difference curves produced using two different extinction coefficients as labeled. Left insets: Images of the sample before (left) and after melting (right). A confocal pinhole is also imaged in the photograph on the right-hand side that collimates the field of view to ~10 μm. Right inset: Extinction coefficient measured through the sample after quenching the melt (dark area in the center of the pinhole) assuming cylindrical shape of the melted region with a total thickness of $2z = 16.4$ μm (measured by SEM). The ambiguity in extinction coefficient due to the assumption of its cylindrical shape is < 10%.

times higher compared to that prior to melting (both at 50 GPa/300 K). Because we cannot disentangle the relative contributions from scattering and absorption we tentatively suppose that the large increase in the extinction coefficient is due to both processes. The grain size of the quenched sample has not been quantitatively constrained in the present work but is likely small. To cite but one example, a grain size of < 500 nm is characteristic of a Bgm-bearing sample recovered in melting experiment in LH DACs (Fiquet et al., 2010). For such a grain size, the forward component of scattering is decreased (Hulst, 1957); thus, the scattering contribution to the extinction coefficient is likely higher than in the above case of translucent Bgm. The steep edge-like increase of the extinction coefficient at $\lambda < 650$ nm in the quenched sample could also be consistent with increased light scattering at grain boundaries. This assignment, however, is not unique as the steep edge-like structure can be assigned to light absorption by the Fe-O CT excitations in Fe-enriched Bgm (Goncharov et al., 2008). The band at ~700–750 nm is most likely related to an absorption process (as opposed to light scattering) because of its relatively small width. We tentatively assign this band to a Fe^{2+}-Fe^{3+} CT although the center of the band is at lower wavelengths than prior to melting the sample.

3.4. Radiometric Temperature Determination in Dark Bgm

Figure 4 (left) shows a representative thermal radiation spectrum collected from the dark area. The corresponding constant emissivity Planck fit yields $T_{apparent} = 2676$ K and a statistical uncertainty of < 1 K. The difference curve changes its sign at ~610, 700, and 790 nm but, overall, the residual is small (<1 %). Below, we will evaluate the models representing this experimental case by their ability to reproduce the sign, change of sign, and amplitude of this residual.

The geometrical parameters used in the modeling are fixed to $d = 11$ μm, $z = 8.2$ μm based on direct measurements in decompressed sample (Figure S1). Unfortunately, the emissivity of dark Bgm cannot be accurately constrained from the experimental data as the scattering contribution to the total measured

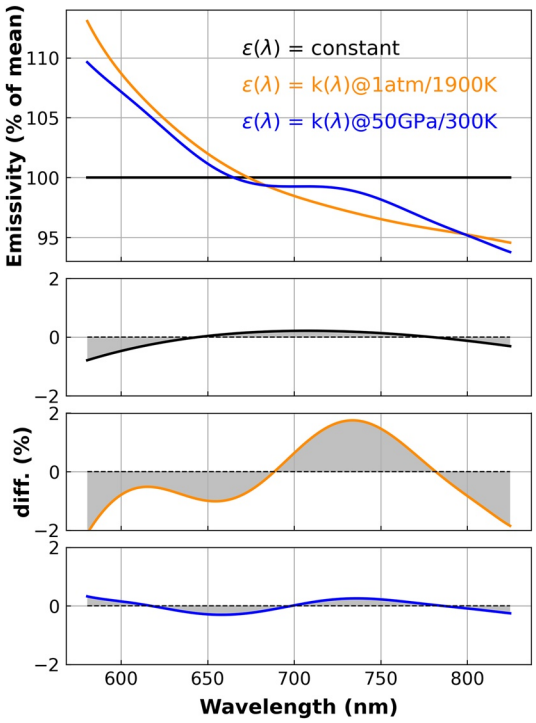

Figure 5. Top: Three qualitative emissivity models of dark Bgm: constant emissivity (black), based on the absorbance of translucent Bgm at 1 atm and 1900 K (orange), and based on the extinction coefficient of dark Bgm measured at 300 K after melting at ~50 GPa (blue). Bottom three panels: Three difference curves (fit/modeled – 1) in % obtained with the three emissivity models while satisfying $T_{apparent} = 2676$ K.

extinction coefficient is unknown. To overcome this problem, we evaluated three models with distinct forms of sample's emissivity that may have relevance to the present case (Figure 5, top). For each choice of emissivity, we adjusted T_{max} to yield $T_{apparent} = 2676$ K at which point the difference curve was compared to the experimental one.

In the first case, we modeled the behavior of a gray sample by fixing the emissivity to a constant and the extinction coefficient to 1750 cm^{-1} (roughly the average of the measured value). Not surprisingly, the resulting difference curve fails to reproduce the experimental one (Figure 5, black difference curve). Nonetheless, this is a useful test as it isolates the systematic error in temperature determination due to the axial temperature gradient in the sample (see Section 3.2). Here, we satisfied the condition of $T_{apparent} = 2676$ K at $T_{max} = 2865$ K, that is the systematic error in measured T is ~7%. This estimate is not universal as it is sensitive to sample geometry, the form of the axial temperature gradient, and the magnitude of the extinction coefficient. In the second case, we employed the emissivity of translucent Bgm given by its extinction coefficient at 1 atm/1900 K. Again, the modeled difference curve (Figure 5, orange difference curve) fails to reproduce the sign of the experimental difference curve at $\lambda < 620$ nm and the maximum amplitudes. The third choice of emissivity was assuming that for dark Bgm $\alpha(\lambda) = k(\lambda)$, which results in emissivity that follows the flexes observed in the measured extinction coefficient. This choice of emissivity performs well yielding the difference curve of correct sign, wavelengths of the change in sign, and amplitude of ~2/3 that in experiment (Figure 5, blue difference curve). The success of this emissivity model suggests that $\alpha(\lambda) >> s(\lambda)$, which is expected because the iron content of Bgm quenched from the melt is higher than that prior to melting. The third choice of emissivity works best because it accounts for the band at ~700–750 nm which, as we discussed above, is likely related to light absorption, making it a reasonable approximation to sample's true emissivity. Overall, the comparison of the difference curves modeled with three distinct forms of emissivity suggests that sample's nongray behavior is dominated by both wavelength-dependent emissivity and light attenuation.

To improve the agreement between the model and experiment we adopted the third form of emissivity and investigated the effect of individual model parameters on the difference curve. As in the case of translucent Bgm, the difference curve is most sensitive to the magnitude of the extinction coefficient. Using the room-temperature extinction coefficient we obtained a difference curve in agreement with the experiment except the modeled amplitude is ~2/3 lower (Figures 4 and 5, blue curve in the bottom panel). However, light absorption in Bgm (and other iron-bearing silicates) is continuously enhanced with heating as the UV absorption edge red-shifts into the visible range (Lobanov et al., 2017; Shankland et al., 1979; Ullrich et al., 2002). For example, the absorption coefficient of Bgm at $T >$ ~2000 K increases by ~0.4–1 cm^{-1}/K (Lobanov, Holtgrewe, et al., 2020; Lobanov et al., 2021). Accepting a temperature-induced increase in the extinction coefficient (due to temperature-enhanced absorption) of 1000 cm^{-1} we generate a difference curve that is very similar to the experimental one (Figure 4, red line in the bottom panel). The condition of $T_{apparent} = 2676$ K is satisfied for $T_{max} = 2975$ K. That is, the fitted temperature observed in the experiment underestimates the maximum temperature in the center of the LH DAC by ~10%. At this point it is convenient to depart from the parabolic temperature profile and explore the effect of the shape of axial temperature gradient on the modeled T_{max}. A near-linear axial temperature gradient can be realized when the thermal insulation is ineffective (Kiefer & Duffy, 2005). Keeping all other parameters fixed (e.g., emissivity profile, geometry) and imposing a linear axial temperature profile, we satisfy the condition of $T_{apparent} = 2676$ K at $T_{max} = 3152$ K. Therefore, the fitted temperature may underestimate the maximum temperature in dark Bgm by up to ~15% in the case of a linear axial temperature profile.

4. Discussion

We showed that two distinct scenarios are characteristic of radiometric temperature determination in Bgm laser-heated in a DAC. The first scenario represents translucent Bgm such as in the case of a single-crystalline or polycrystalline sample with a relatively large grain size (> 2 μm). For such a case, our results show that the usual assumption of $T_{apparent} = T_{max}$ in LH DAC experiments results in the overestimation of T_{max} in the sample by up to 5% (at $T_{max} < 2000$ K). The amplitude of the difference curve shows significant deviations of up to ~10% (Figure 2). This relatively large amplitude of the difference curve is due to sample's rapidly increasing emissivity at $\lambda < \sim 650$ nm (red curve in the top panel of Figure 5) while the extinction coefficient is too low to significantly attenuate the extra light. We expect that this scenario holds in the limit of Bgm with relatively low Fe content (e.g., 5 mol. % Fe used here) but may reverse as the extinction coefficient is increased at higher Fe concentrations and the wavelength-dependent light attenuation becomes more important. The second scenario sets in when sample's extinction coefficient is high and prevents the extra short-wavelength light from reaching the detector, the direct consequence of which is the small maximum amplitude of the difference curve (<1%, Figure 4). In spite of the good fit, the apparent temperature systematically underestimates T_{max} by ~10%. Therefore, the small amplitude of the difference curve is deceiving and does not validate the graybody assumption. A two-color pyrometer fit to the experimentally-observed thermal emission spectrum helps to identify problems in Planck-fitting under the graybody assumption (Figure S5) as is indicated by a large spread of the two-color temperature both below and above $T_{apparent}$. However, it does not allow addressing the magnitude of temperature underestimation that results from the graybody assumption. The latter requires quantitative information on the sample's optical properties at high *P-T* conditions which can be measured (as in this study) or computed (Lobanov et al., 2021).

In both scenarios a closer resemblance of the experimental and modeled difference curves was achieved by modifying the optical properties of Bgm by a constant (see red modeled curves in the bottom right panels of Figures 3 and 4). However, the physical justification for such a correction was different. In the case of translucent Bgm, it serves to account for light scattering as opposed to temperature-induced changes in the extinction coefficient in the case of dark Bgm. Such a simple correction is convenient and potentially accounts for multiple experimentally-unconstrained factors that affect light transport in a real laser-heated DAC experiment. These include deviations from the assumed *T* profile, varying optical properties along the axial *T* profile, spectral contributions of colder regions along the radial *T* gradient, sample thickness and its actual shape, and non-symmetrical sample position in the cavity.

The practical outcome of the present work is that it shows that radiometric temperature determination under the graybody assumption may introduce a potentially significant error to the phase diagram of Bgm (up to 10% in *T*). The case of translucent Bgm is representative of radiometric temperature determination in LH DAC experiments at $T < T_{solidus}$ (i.e., prior to melting the sample). This is the temperature regime of some previous studies of the Bgm-Ppv phase boundary that were based on the graybody-fit to the spectrum emitted by the hot silicate sample (Catalli et al., 2009; Sun et al., 2018). We estimated the difference between T_{max} and $T_{apparent}$ in the case of a hypothetical experiment performed at $P \sim 120$ GPa and graybody temperature ($T_{apparent}$) = 2500 K (which roughly corresponds to the Bgm-Ppv crossover) by accepting the 1 atm/1900 K extinction coefficient of translucent Bgm and sample geometry characteristic of DAC experiments at $P > 100$ GPa ($d = 2.5$ μm, $z = 2.0$ μm). The use of this extinction coefficient is adequate to first order for reasons discussed in Section 3.1. If the optical properties of Bgm/Ppv at the core-mantle boundary (CMB) are those of Bgm at 1 atm and 1900 K, then T_{max} and $T_{apparent}$ are within 0.5%; that is, negligible systematic error in temperature determination. However, we also consider the effect of plausible minor *T*- or *P*-induced changes in the absorption coefficient of Bgm by allowing it to vary in the limit of ±100 cm^{-1} (i.e., overall increase or decrease in the coefficient). Temperature-induced changes in the absorption coefficient of Bgm are wavelength-dependent and may be both positive and negative in visible and near-IR range with the net effect of ~0.05 cm^{-1}/K at T < ~2500 K (Lobanov et al., 2021). This is compatible with the reported *T*- and *P*- changes in optical absorption of other ferromagnesian minerals at $T < \sim 2000$ K (Lobanov, Holtgrewe, et al., 2020; Lobanov et al., 2017; Ullrich et al., 2002). The purpose of considering a wavelength-independent change in the coefficient by ±100 cm^{-1} is to bracket the systematic error in the experimental *T* determination of the Bgm/Ppv phase transition due to nongray but yet not fully constrained optical properties of Bgm/Ppv at *P-T* conditions representative of the CMB. We found that under these model parameters the

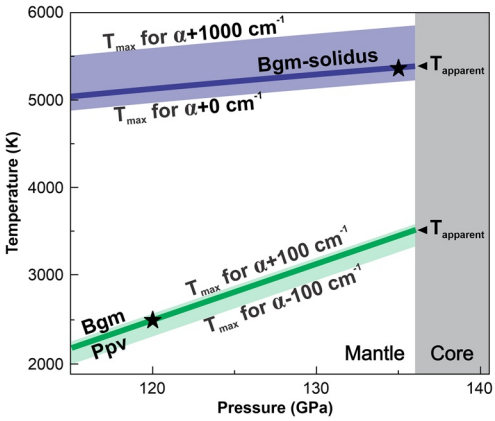

Figure 6. Possible systematic error in the phase diagram of translucent Bgm due to its nongray optical properties (light green and blue areas). Black stars are $T_{apparent}$ used in the modeling of T_{max}, which are shown as bounds around the Bgm-Ppv transition and Bgm solidus. These bounds illustrate the importance of optical properties of Bgm (or Ppv) in constraining the phase diagram. The numbers near the bounds depict possible but yet unconstrained *P*- and *T*-induced changes in the (experimentally-based) extinction coefficient of Bgm used in modeling T_{max} (as described in the text). The Bgm-Ppv phase boundary (green solid line) has the same pressure dependence as measured by Tateno et al. (2009) for pure $MgSiO_3$ but shifted to qualitatively represent the effect of Fe-Mg substitution (Hirose et al., 2017). The solidus of Bgm is shown by a blue solid curve after Andrault et al. (2017).

apparent temperature may overestimate T_{max} by up to ~8% (for a decrease in α of 100 cm^{-1}) or underestimate T_{max} by up to ~2% (for an increase in α of 100 cm^{-1}). These modeling results are schematically depicted in Figure 6 as the light green band, representing a plausible range of systematic error introduced by the graybody approximation in reference to the Bgm-Ppv boundary (solid green line). While our modeled bounds would still be consistent with the Ppv interpretation of the D″ seismic discontinuities, the presented case illustrates that optical properties of the Bgm-Ppv system at near-CMB conditions are needed for a more rigorous determination of the Bgm-Ppv phase transition, especially when multiphase mantle-like samples are investigated in the LH DAC.

In a similar way we can estimate the potential error in the position of the experimental Bgm solidus curve based on graybody Planck fitting in LH DACs. In experiments to constrain $T_{solidus}$ one may record radiometric temperatures upon gradually increasing the laser heating power. In such a case, temperatures recorded prior to the onset of melting constrain the lower bound on $T_{solidus}$. Using the 1 atm/1900 K extinction coefficient of translucent Bgm, we obtained that *Tmax* is ~3% lower than $T_{apparent}$ = 5200 K at CMB (P = 135 GPa). However, due to the vast difference between our experimental conditions (1 atm/1900 K) and those at the CMB, we need to account for the likely positive temperature dependence of the absorption coefficient of Bgm at high temperature of ~0.4 cm^{-1}/K at T > 2000 K (Lobanov et al., 2021). By accepting that α increases by 1000 cm^{-1}, we obtained that T_{max} is ~9% higher than $T_{apparent}$ = 5200 K (Figure 6). While these models allow only semiquantitative inferences, they urge a new approach in determining/evaluating radiometric Bgm-Ppv phase transition temperatures as well as melting temperatures of Bgm-rich samples in LH DACs that accounts for sample's optical properties constrained at high *P-T*.

5. Conclusions

We showed that the deviations of measured thermal emission from an ideal graybody behavior carry information on the interaction of light with the hot nongray Bgm in a LH DAC. Temperatures measured in LH DAC experiments on Bgm may both underestimate and overestimate the maximum temperature in the sample, depending on its optical properties. In our experiments we find that the difference between sample's maximum and measured temperatures in LH DAC experiments is resolvable and can be corrected through modeling the emission and transport of thermal radiation in the sample with established wavelength-dependent optical properties. Extrapolating the results of the present work, including qualitative pressure and temperature effects, to lowermost mantle and core-mantle boundary conditions shows that consequences of this previously unaccounted error in the phase diagram of Bgm may be significant. Our study, therefore, warrants a careful re-evaluation of phase boundaries in the Bgm system enabled by its optical properties constrained at appropriate *P-T* conditions.

Conflict of Interest

The authors declare no conflict of interest.

Data Availability Statement

Spectroscopic data associated with this paper are deposited at Mendeley Data (https://doi.org/10.17632/6xy3dxb4b5.1).

Acknowledgments
S. S. L. and L. S. acknowledge the support of the Helmholtz Young Investigators Group CLEAR (VH-NG-1325). J. F. L. acknowledges support from Geophysics Program of the National Science Foundation of the United States (EAR-1916941 and EAR-2001381). The authors thank T. Okuchi, N. Purevjav, and S. Fu for help with the sample synthesis and preparation. Likewise, Xinyang Li is thanked for his assistance in collecting x-ray diffraction data. We thank Sylvain Petitgirard, anonymous reviewers, and the editors for helping us to improve this work.
Open access funding enabled and organized by Projekt DEAL.

References

Akahama, Y., & Kawamura, H. (2006). Pressure calibration of diamond anvil Raman gauge to 310 GPa. *Journal of Applied Physics*, *100*(4), 043516. https://doi.org/10.1063/1.2335683

Andrault, D., Bolfan-Casanova, N., Bouhifd, M. A., Boujibar, A., Garbarino, G., Manthilake, G., et al. (2017). Toward a coherent model for the melting behavior of the deep Earth's mantle. *Physics of the Earth and Planetary Interiors*, *265*, 67–81. https://doi.org/10.1016/j.pepi.2017.02.009

Andrault, D., Bolfan-Casanova, N., Lo Nigro, G., Bouhifd, M. A., Garbarino, G., & Mezouar, M. (2011). Solidus and liquidus profiles of chondritic mantle: Implication for melting of the Earth across its history. *Earth and Planetary Science Letters*, *304*(1–2), 251–259. https://doi.org/10.1016/j.epsl.2011.02.006

Andrault, D., Pesce, G., Bouhifd, M. A., Bolfan-Casanova, N., Henot, J.-M., & Mezouar, M. (2014). Melting of subducted basalt at the core-mantle boundary. *Science*, *344*(6186), 892–895. https://doi.org/10.1126/science.1250466

Benedetti, L. R., Guignot, N., & Farber, D. L. (2007). Achieving accuracy in spectroradiometric measurements of temperature in the laser-heated diamond anvil cell: Diamond is an optical component. *Journal of Applied Physics*, *101*(1), 013109. https://doi.org/10.1063/1.2402587

Benedetti, L. R., & Loubeyre, P. (2004). Temperature gradients, wavelength-dependent emissivity, and accuracy of high and very-high temperatures measured in the laser-heated diamond cell. *High Pressure Research*, *24*(4), 423–445. https://doi.org/10.1080/08957950412331331718

Boltzmann, L. (1884). Ableitung des Stefan'schen Gesetzes, betreffend die Abhängigkeit der Wärmestrahlung von der Temperatur aus der electromagnetischen Lichttheorie. *Annals of Physics*, *258*, 291–294. https://doi.org/10.1002/andp.18842580616

Campbell, A. J. (2008). Measurement of temperature distributions across laser heated samples by multispectral imaging radiometry. *Review of Scientific Instruments*, *79*(1), 015108. https://doi.org/10.1063/1.2827513

Catalli, K., Shim, S.-H., & Prakapenka, V. (2009). Thickness and Clapeyron slope of the post-perovskite boundary. *Nature*, *462*(7274), 782–785. https://doi.org/10.1038/nature08598

Deng, J., Du, Z. X., Benedetti, L. R., & Lee, K. K. M. (2017). The influence of wavelength-dependent absorption and temperature gradients on temperature determination in laser-heated diamond-anvil cells. *Journal of Applied Physics*, *121*(2), 025901. https://doi.org/10.1063/1.4973344

Deng, J., & Lee, K. K. M. (2017). Viscosity jump in the lower mantle inferred from melting curves of ferropericlase. *Nature Communications*, *8*. 1997. https://doi.org/10.1038/s41467-017-02263-z

Du, Z. X., Amulele, G., Benedetti, L. R., & Lee, K. K. M. (2013). Mapping temperatures and temperature gradients during flash heating in a diamond-anvil cell. *Review of Scientific Instruments*, *84*(7), 075111. https://doi.org/10.1063/1.4813704

Fiquet, G., Auzende, A. L., Siebert, J., Corgne, A., Bureau, H., Ozawa, H., & Garbarino, G. (2010). Melting of Peridotite to 140 Gigapascals. *Science*, *329*(5998), 1516–1518. https://doi.org/10.1126/science.1192448

Fu, S., Yang, J., Zhang, Y., Okuchi, T., McCammon, C., Kim, H.-I., et al. (2018). Abnormal elasticity of Fe-bearing Bridgmanite in the Earth's lower mantle. *Geophysical Research Letters*, *45*(10), 4725–4732. https://doi.org/10.1029/2018gl077764

Garnero, E. J. (2000). Heterogeneity of the lowermost mantle. *Annual Review of Earth and Planetary Sciences*, *28*, 509–537. https://doi.org/10.1146/annurev.earth.28.1.509

Geballe, Z. M., Sime, N., Badro, J., van Keken, P. E., & Goncharov, A. F. (2020). Thermal conductivity near the bottom of the Earth's lower mantle: Measurements of pyrolite up to 120 GPa and 2500 K. *Earth and Planetary Science Letters*, *536*, 116161. https://doi.org/10.1016/j.epsl.2020.116161

Giampaoli, R., Kantor, I., Mezouar, M., Boccato, S., Rosa, A. D., Torchio, R., et al. (2018). Measurement of temperature in the laser heated diamond anvil cell: Comparison between reflective and refractive optics. *High Pressure Research*, *38*(3), 250–269. https://doi.org/10.1080/08957959.2018.1480017

Goncharov, A. F., Haugen, B. D., Struzhkin, V. V., Beck, P., & Jacobsen, S. D. (2008). Radiative conductivity in the Earth's lower mantle. *Nature*, *456*(7219), 231–234. https://doi.org/10.1038/nature07412

Goncharov, A. F., Lobanov, S. S., Tan, X., Hohensee, G. T., Cahill, D. G., Lin, J.-F., et al. (2015). Experimental study of thermal conductivity at high pressures: Implications for the deep Earth's interior. *Physics of the Earth and Planetary Interiors*, *247*, 11–16. https://doi.org/10.1016/j.pepi.2015.02.004

Goncharov, A. F., Struzhkin, V. V., & Jacobsen, S. D. (2006). Reduced radiative conductivity of low-spin (Mg,Fe)O in the lower mantle. *Science*, *312*(5777), 1205–1208. https://doi.org/10.1126/science.1125622

Goncharov, A. F., Struzhkin, V. V., Montoya, J. A., Kharlamova, S., Kundargi, R., Siebert, J., et al. (2010). Effect of composition, structure, and spin state on the thermal conductivity of the Earth's lower mantle. *Phys. Earth Planet. Inter.*, *180*(3–4), 148–153. https://doi.org/10.1016/j.pepi.2010.02.002

Heinz, D. L., & Jeanloz, R. (1987a). Measurement of the melting curve of Mg0.9Fe0.1 SiO3 at lower mantle conditions and its geophysical implications. *Journal of Geophysical Research*, *92*(B11), 11437–11444. https://doi.org/10.1029/jb092ib11p11437

Heinz, D. L., & Jeanloz, R. (1987b). Temperature measurements in the laser-heated diamond cell. In M. H. Manghnani, & Y. Syono (Eds.), *High-pressure research in mineral physics: A volume in honor of Syun-iti Akimoto* (pp. 113–127). American Geophysical Union. https://doi.org/10.1029/GM039p0113

Hernlund, J. W., Thomas, C., & Tackley, P. J. (2005). A doubling of the post-perovskite phase boundary and structure of the Earth's lowermost mantle. *Nature*, *434*(7035), 882–886. https://doi.org/10.1038/nature03472

Hirose, K., Sinmyo, R., & Hernlund, J. (2017). Perovskite in Earth's deep interior. *Science*, *358*(6364), 734–738. https://doi.org/10.1126/science.aam8561

Holtgrewe, N., Greenberg, E., Prescher, C., Prakapenka, V. B., & Goncharov, A. F. (2019). Advanced integrated optical spectroscopy system for diamond anvil cell studies at GSECARS. *High Pressure Research*, *39*(3), 457–470. https://doi.org/10.1080/08957959.2019.1647536

Hulst, H. C. V. D. (1957), *Light scattering by small particles*, 470 p., Wiley.

Irifune, T., Shinmei, T., McCammon, C. A., Miyajima, N., Rubie, D. C., & Frost, D. J. (2010). Iron Partitioning and Density Changes of Pyrolite in Earth's Lower Mantle. *Science*, *327*(5962), 193–195. https://doi.org/10.1126/science.1181443

Jeanloz, R., & Heinz, D. L. (1984). Experiments at high temperature and pressure – Laser heating through the diamond cell. *Journal of De Physique*, *45*(11). https://doi.org/10.1051/jphyscol:1984817

Kavner, A., & Panero, W. R. (2004). Temperature gradients and evaluation of thermoelastic properties in the synchrotron-based laser-heated diamond cell. *Physics of the Earth and Planetary Interiors*, *143–144*, 527–539. https://doi.org/10.1016/j.pepi.2003.12.016

Keppler, H., Dubrovinsky, L. S., Narygina, O., & Kantor, I. (2008). Optical absorption and radiative thermal conductivity of silicate perovskite to 125 Gigapascals. *Science*, *322*(5907), 1529–1532. https://doi.org/10.1126/science.1164609

Keppler, H., Mccammon, C. A., & Rubie, D. C. (1994). Crystal-field and charge-transfer spectra of (Mg,Fe)SiO_3 perovskite. *American Mineralogist*, *79*(11–12), 1215–1218.

Kiefer, B., & Duffy, T. S. (2005). Finite element simulations of the laser-heated diamond-anvil cell. *Journal of Applied Physics*, *97*(11), 114902. https://doi.org/10.1063/1.1906292

Kirchhoff, G. (1860). Ueber das Verhältniss zwischen dem Emissionsvermögen und dem Absorptionsvermögen der Körper für Wärme und Licht. *Annals of Physical Chemistry*, *185*, 275–301. https://doi.org/10.1002/andp.18601850205

Kirchhoff, G. (1861). On a new proposition in the Theory of Heat. *Philosophical Magazine*, *21*, 241–247.

Kunz, M., Yan, J. Y., Cornell, E., Domning, E. E., Yen, C. E., Doran, A., et al. (2018). Implementation and application of the peak scaling method for temperature measurement in the laser heated diamond anvil cell. *Review of Scientific Instruments*, *89*(8), 083903. https://doi.org/10.1063/1.5028276

Lay, T., Hernlund, J., & Buffett, B. A. (2008). Core-mantle boundary heat flow. *Nature Geosci*, *1*(1), 25–32. https://doi.org/10.1038/ngeo.2007.44

Lobanov, S. S., Holtgrewe, N., & Goncharov, A. F. (2016). Reduced radiative conductivity of low spin FeO6-octahedra in FeCO3 at high pressure and temperature. *Earth and Planetary Science Letters*, *449*, 20–25. https://doi.org/10.1016/j.epsl.2016.05.028

Lobanov, S. S., Holtgrewe, N., Ito, G., Badro, J., Piet, H., Nabiei, F., et al. (2020). Blocked radiative heat transport in the hot pyrolitic lower mantle. *Earth and Planetary Science Letters*, *537*, 116176. https://doi.org/10.1016/j.epsl.2020.116176

Lobanov, S. S., Holtgrewe, N., Lin, J.-F., & Goncharov, A. F. (2017). Radiative conductivity and abundance of post-perovskite in the lowermost mantle. *Earth and Planetary Science Letters*, *479*, 43–49. https://doi.org/10.1016/j.epsl.2017.09.016

Lobanov, S. S., Schifferle, L., & Schulz, R. (2020). Gated detection of supercontinuum pulses enables optical probing of solid and molten silicates at extreme pressure-temperature conditions. *Review of Scientific Instruments*, *91*(5). https://doi.org/10.1063/5.0004590

Lobanov, S. S., Soubiran, F., Holtgrewe, N., Badro, J., Lin, J.-F., & Goncharov, A. F. (2021). Contrasting opacity of bridgmanite and ferropericlase in the lowermost mantle: Implications to radiative and electrical conductivity. *Earth and Planetary Science Letters*, *562*, 116871. https://doi.org/10.1016/j.epsl.2021.116871

Lobanov, S. S., & Speziale, S. (2019). Radiometric temperature measurements in nongray ferropericlase with pressure- spin- and temperature-dependent optical properties. *Journal of Geophysical Research: Solid Earth*, *124*, 12825–12836. https://doi.org/10.1029/2019jb018668

Manga, M., & Jeanloz, R. (1996). Axial temperature gradients in dielectric samples in the laser-heated diamond cell. *Geophysical Research Letters*, *23*(14), 1845–1848. https://doi.org/10.1029/96gl01602

Mattson, S. M., & Rossman, G. R. (1987). Identifying characteristics of charge transfer transitions in minerals. *Physics and Chemistry Minerals*, *14*(1), 94–99. https://doi.org/10.1007/bf00311152

McMahon, H. O. (1950). Thermal radiation from partially transparent reflecting bodies. *Journal of the Optical Society of America*, *40*(6), 376–380. https://doi.org/10.1364/josa.40.000376

Montoya, J. A., & Goncharov, A. F. (2012). Finite element calculations of the time dependent thermal fluxes in the laser-heated diamond anvil cell. *Journal of Applied Physics*, *111*(11), 112617. https://doi.org/10.1063/1.4726231

Moore, M. M., Garnero, E. J., Lay, T., & Williams, Q. (2004). Shear wave splitting and waveform complexity for lowermost mantle structures with low-velocity lamellae and transverse isotropy. *Journal of Geophysical Research: Solid Earth*, *109*(B2). https://doi.org/10.1029/2003jb002546

Murakami, M., Hirose, K., Kawamura, K., Sata, N., & Ohishi, Y. (2004). Post-Perovskite phase transition in $MgSiO_3$. *Science*, *304*(5672), 855–858. https://doi.org/10.1126/science.1095932

Nomura, R., Hirose, K., Uesugi, K., Ohishi, Y., Tsuchiyama, A., Miyake, A., & Ueno, Y. (2014). Low core-mantle boundary temperature inferred from the solidus of pyrolite. *Science*, *343*(6170), 522–525. https://doi.org/10.1126/science.1248186

Oganov, A. R., & Ono, S. (2004). Theoretical and experimental evidence for a post-perovskite phase of MgSiO3 in Earth's D″ layer. *Nature*, *430*(6998), 445–448. https://doi.org/10.1038/nature02701

Ohta, K., Cohen, R. E., Hirose, K., Haule, K., Shimizu, K., & Ohishi, Y. (2012). Experimental and Theoretical Evidence for Pressure-Induced Metalization in FeO with Rocksalt-Type Structure. *Physical Review Letters*, *108*(2), 026403. https://doi.org/10.1103/physrevlett.108.026403

Panero, W. R., & Jeanloz, R. (2001). Temperature gradients in the laser-heated diamond anvil cell. *Journal of Geophysical Research*, *106*(B4), 6493–6498. https://doi.org/10.1029/2000jb900423

Petitgirard, S., Salamat, A., Beck, P., Weck, G., & Bouvier, P. (2014). Strategies Forin Situlaser heating in the diamond anvil cell at an X-ray diffraction beamline. *Journal of Synchrotron Radiation*, *21*, 89–96. https://doi.org/10.1107/s1600577513027434

Rainey, E. S. G., Hernlund, J. W., & Kavner, A. (2013). Temperature distributions in the laser-heated diamond anvil cell from 3-D numerical modeling. *Journal of Applied Physics*, *114*(20), 204905. https://doi.org/10.1063/1.4830274

Rainey, E. S. G., & Kavner, A. (2014). Peak scaling method to measure temperatures in the laser-heated diamond anvil cell and application to the thermal conductivity of MgO. *Journal of Geophysical Research: Solid Earth*, *119*(11), 8154–8170. https://doi.org/10.1002/2014jb011267

Seagle, C. T., Heinz, D. L., Liu, Z., & Hemley, R. J. (2009). Synchrotron infrared reflectivity measurements of iron at high pressures. *Applied Optics*, *48*(3), 545–552. https://doi.org/10.1364/ao.48.000545

Shankland, T. J., Nitsan, U., & Duba, A. G. (1979). Optical absorption and radiative heat transport in olivine at high temperature. *Journal of Geophysical Research*, *84*, 1603–1610. https://doi.org/10.1029/jb084ib04p01603

Shen, G. Y., & Mao, H. K. (2017). High-pressure studies with x-rays using diamond anvil cells. *Reports on Progress in Physics*, *80*(1), 1–53. https://doi.org/10.1088/1361-6633/80/1/016101

Sidorin, I., Gurnis, M., Helmberger, D. V., & Ding, X. M. (1998). Interpreting D″ seismic structure using synthetic waveforms computed from dynamic models. *Earth and Planetary Science Letters*, *163*(1–4), 31–41. https://doi.org/10.1016/s0012-821x(98)00172-1

Stefan, J. (1879). Sitzungsberichte der Kaiserlichen Akademie der Wissenschaften in Wien (79 (pp. 391–428). Über die Beziehung zwischen der Wärmestrahlung und der Temperatur.

Sun, N., Wei, W., Han, S., Song, J., Li, X., Duan, Y., et al. (2018). Phase transition and thermal equations of state of (Fe,Al)-bridgmanite and post-perovskite: Implication for the chemical heterogeneity at the lowermost mantle. *Earth and Planetary Science Letters*, *490*, 161–169. https://doi.org/10.1016/j.epsl.2018.03.004

Tateno, S., Hirose, K., Sata, N., & Ohishi, Y. (2009). Determination of post-perovskite phase transition boundary up to 4400 K and implications for thermal structure in D″ layer. *Earth and Planetary Science Letters*, *277*(1), 130–136. https://doi.org/10.1016/j.epsl.2008.10.004

Touloukian, Y. S., & DeWitt, D. P. (1972). *Thermophysical properties of matter - the TPRC data series* (8. Reannouncement). Data Book Thermal radiative properties - nonmetallic solids.

Ullrich, K., Langer, K., & Becker, K. D. (2002). Temperature dependence of the polarized electronic absorption spectra of olivines. Part I - fayalite. *Physics and Chemistry of Minerals*, *29*(6), 409–419. https://doi.org/10.1007/s00269-002-0248-4

van der Hilst, R. D., de Hoop, M. V., Wang, P., Shim, S.-H., Ma, P., & Tenorio, L. (2007). Seismostratigraphy and thermal structure of Earth's core-mantle boundary region. *Science*, *315*(5820), 1813–1817. https://doi.org/10.1126/science.1137867

Walter, M. J., & Koga, K. T. (2004). The effects of chromatic dispersion on temperature measurement in the laser-heated diamond anvil cell. *Physics of the Earth and Planetary Interiors*, *143–144*, 541–558. https://doi.org/10.1016/j.pepi.2003.09.019

Wang, X., Tsuchiya, T., & Hase, A. (2015). Computational support for a pyrolitic lower mantle containing ferric iron. *Nature Geosci*, *8*(7), 556–559. https://doi.org/10.1038/ngeo2458

Yeganeh-Haeri, A. (1994). Synthesis and re-investigation of the elastic properties of single-crystal magnesium silicate perovskite. *Physics of the Earth and Planetary Interiors*, *87*(1), 111–121. https://doi.org/10.1016/0031-9201(94)90025-6

Zerr, A., & Boehier, R. (1993). Melting of (Mg, Fe)SiO3-Perovskite to 625 kilobars: Indication of a high melting temperature in the lower mantle. *Science*, *262*(5133), 553–555. https://doi.org/10.1126/science.262.5133.553